PAPER

A minimally designed soft crawling robot for robust locomotion in unstructured pipes

Bioinspiration & Biomimetics

PAPER

A minimally designed soft crawling robot for robust locomotion in unstructured pipes

RECEIVED
27 March 2022

REVISED
26 May 2022

ACCEPTED FOR PUBLICATION
30 May 2022

PUBLISHED
8 July 2022

Wenkai Yu[1], Xin Li[1], Dunyu Chen[1], Jingyi Liu[1], Jiaji Su[2], Ju Liu[1], Changyong Cao[2] and Hongyan Yuan[1,*]

[1] Shenzhen Key Laboratory of Soft Mechanics & Smart Manufacturing, Department of Mechanics and Aerospace Engineering, Southern University of Science and Technology, Shenzhen, 518055, People's Republic of China
[2] Laboratory for Soft Machines & Electronics, Department of Mechanical and Aerospace Engineering, Case Western Reserve University, Cleveland, OH 44106, United States of America
[*] Author to whom any correspondence should be addressed.

E-mail: yuanhy3@sustech.edu.cn

Keywords: soft crawling robot, tendon-driven, constant curvature, unstructured pipes

Supplementary material for this article is available online

Abstract

Soft robots have attracted increasing attention due to their excellent versatility and broad applications. In this article, we present a minimally designed soft crawling robot (SCR) capable of robust locomotion in unstructured pipes with various geometric/material properties and surface topology. In particular, the SCR can squeeze through narrow pipes smaller than its cross section and propel robustly in spiked pipes. The gait pattern and locomotion mechanism of this robot are experimentally investigated and analysed by the finite element analysis, revealing that the resultant forward frictional force is generated due to the asymmetric mechanical properties along the length direction of the robot. The proposed simple yet working SCR could inspire novel designs and applications of soft robots in unstructured narrow canals such as large intestines or industrial pipelines.

1. Introduction

To mimic the manipulation and locomotion mechanisms of soft biological organisms, soft robots, which are made primarily of materials with a low elastic modulus, have recently attracted intense research interest [1]. Soft robots can deform and conform to their environment [2], and thus are safe to operate when interacting with humans, animals or tissues/organs [3, 4] without sophisticated force control. Their versatility, adaptability and relatively easy control make them suited for open-ended tasks such as navigating in unstructured narrow pipes or cluttered environments.

Among the diverse kinds of soft robots, soft crawling robots (SCRs) have great potential in interventional medical surgeries and industrial pipeline inspections [5]. SCRs typically have the limbless design concept and slender rod-shaped bodies that suit tubular environments. Various locomotion mechanisms have been developed for the limbless SCRs, which can be roughly divided into four categories: anchoring–extension locomotion (figure 1(a)), anisotropic friction-based locomotion (figure 1(b)), heterogeneous friction-based locomotion (figure 1(c)) and the oscillating wave-based locomotion (figure 1(d)).

Anchoring-extension SCRs are mostly inspired by inchworms [6–10], earthworms [11, 12] and snakes. The typical inchworm-like robot usually has three segments: the front, middle and rear segments. The main deformation mode of the three segments is contraction and expansion. The front and rear segments can anchor in the pipe separately, and then the middle segment can extend and contract to make the robot move. The anchoring is achieved by increasing the frictional force via jamming or adhering. The jamming indicates that the robots can expand to increase normal contact force by inflating [7–9] and bulking [10, 13]. Adhering-based robots

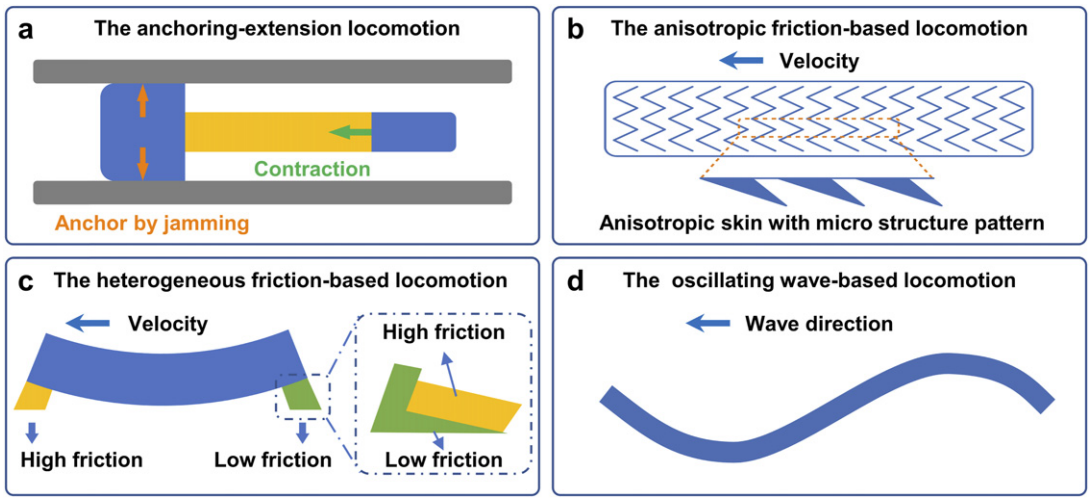

Figure 1. Features of the available locomotion mechanisms for limbless SCRs. (a) Anchoring–extension design. (b) Anisotropic friction-based design. (c) Heterogeneous friction-based design. (d) Oscillating wave-based design.

can attach to a surface tightly by vacuum-induced suction [11, 14, 15] or controlled adhesion [16, 17]. Anchoring–extension robots are popular due to their excellent adaptability to pipes with even surfaces. However, they are inapposite for uneven or spiked pipes.

Anisotropic friction-based SCRs have an anisotropic frictional skin generated by a covered origami structure [12, 18, 19] or a microstructure pattern [20], while heterogeneous friction-based locomotion relies on heterogeneous but isotropic frictional skin [21–24] to generate non-uniform friction coefficient distribution along the robot body. The unbalanced friction due to the unique frictional property enables these SCRs to move in a simple gait pattern but with an improved locomotion efficiency. However, the fabrication and the bi-directional locomotion of such robots are relatively complicated.

Oscillating wave-based SCRs usually have multiple segments that can bend separately to form a wave-like gait pattern. With an isotropic frictional skin [25, 26], they can generate a propelling force through the designed gait pattern, like a serpentine wave [26, 27]. Compared with heterogeneous friction-based locomotion, the oscillating wave-based design is more straightforward, but the number of segments or the length to realize efficient locomotion need to be determined. Whether a crawling robot with one segment is sufficient to realize locomotion is unclear.

Similarly, a variety of actuation approaches have been developed for SCRs, such as tendon-driven [6, 10, 28–30], pneumatic-/hydraulic-driven [9, 14, 19, 21, 31] and smart material-driven (including dielectric elastomer [16], shape-memory alloy [22–24] and magnetic material [32–34]). The actuation strategies determine the main deformation modes for SCRs, i.e. bending, contraction and expansion. The pneumatic/hydraulic driven approach is the most common, with lightweight, non-electronic components and high environmental adaptability features. It generally requires high pressure or sophisticated design to achieve large deformation in specific directions. The smart material-driven method has the advantages of high energy density and low noise but is constrained by its material properties. For example, shape-memory alloys cause significant thermal effects and have a relatively low deformation rate. In addition, the complex configuration of driven fields like high-voltage generators or Helmholtz coils also limits their broad applications. The tendon-driven method has promising features, such as direct and efficient force transmission, and relatively simple mechanical design, fabrication and kinematic modeling, and it has been widely applied in continuum manipulators [35] and artificial fingers [36], but rarely adopted in crawling robots.

In practice, the geometrical, topological and mechanical properties of the environment can change dramatically, which poses significant challenges for SCRs to adapt to uncertain terrains. For instance, the dimensions of an unstructured pipe are irregular and may vary dramatically along its length, or may be even smaller than the crawling robot. If spiked surfaces are encountered, pneumatic/hydraulic-driven soft robots may be easily damaged or punctured. Current SCRs are mainly designed for structured pipes that are even, rigid and dry [6, 10, 31, 37]. Although some recent worm-like crawling robots attempted to locomote in complicated environments [9, 37, 38], they are still unable to crawl in unstructured challenging conditions such as being stuck or pipes with spiked surfaces. Moreover, to better accommodate unstructured environments, SCRs should be miniature, lightweight and reliable. Therefore, it is highly desirable to design a tendon-driven SCR to keep the above merits and improve its adaptability and robustness.

In this article, a soft and robust tendon-driven crawling robot with a minimalist design, which only

Table 1. Comparison of our SCR with other crawling robots[a].

Ref	Criterion						
	Actuation Deformation mode	Locomotion mechanism	Speed Max speed Body length (BL) BL s^{-1}	Load-carrying capacity	Max load Robot weight Max load/robot weight	The width of pipe	Range of width Robot width (BW) Width range/BW
Our SCR	Tendon-driven One bending segment	Oscillating wave with asymmetric design	10 mm s^{-1} 148 mm 0.0676 BL s^{-1}	1560 g 78 g 20		28 mm 25–80 mm 0.89–2.85	
Bernth *et al* [6]	Tendon-driven Three bending segments	Anchoring-extension	1.21 mm s^{-1} 500 mm 2.42 × 10^{-3} BL s^{-1}	—		26 mm 26–50 mm 1–1.92	
Liu *et al* [7]	Pneumatic-driven One contraction and two expansion segments	Anchoring-extension	5 mm s^{-1} 43 mm 0.1163 BL s^{-1}	1000 g 85.4 g 11.71		50 mm 50–65 mm 1–1.30	
Zhang *et al* [9]	Pneumatic-driven One contraction and two expansion segments	Anchoring-extension	— 80 mm —	157.3 g 14.5 g 10.85		15 mm 15–25 mm 1–1.67	
Rafsanjani *et al* [19]	Pneumatic-driven One contraction segment	Anisotropic friction	8.5 mm s^{-1} 164 mm 0.0518 BL s^{-1}	—		25 mm 25–∞ mm 1–∞	
Qi *et al* [26]	Pneumatic-driven Four bending segments	Oscillating wave	35 mm s^{-1} — —	—		— 41–152 mm —	

[a]Not mentioned in the reference.

needs a single motor to achieve bending wave and realize locomotion in unstructured pipes, is presented. A constant curvature model considering axial contraction is developed to model the kinematic deformation of the soft tendon-driven robot. The gait pattern and locomotion mechanism are experimentally investigated and validated by finite element analysis (FEA). The locomotion experiments in unstructured pipes are performed under different working conditions, including in a trapped or spiked pipe. Our conclusions and future studies are then discussed.

To highlight the performance of the proposed SCR, a comparison of our SCR and other crawling robots in the literature was conducted in terms of actuation strategy, locomotion mechanism with deformation mode, speed performance, load-carrying capacity and the width/diameter of pipe it can propel, as shown in table 1. The design parameters of the robot, such as body length (BL), body width (BW) and robot weight, have a significant impact on its performance. Therefore, the ratios of robot performance to its relevant design parameters, such as BL per second, the ratio of max load to self-weight and the ratio of pipe width to BW, are defined as reasonable criteria for evaluating the robot's performance. The load-carrying capacity of our SCR performs well, up to 20 times the robot's weight, although its maximum speed performance is 0.0676 BL s^{-1}. Our SCR can propel effectively in pipes with a wide range of width, ranging from 25 mm to 80 mm (0.89–2.58 times BW).

2. Design, fabrication and modeling of the SCR

2.1. Minimalist mechanical design and fabrication

As shown in figure 2(a), the proposed SCR consists of three segments, the front segment (i.e. robot head), the middle segment (i.e. robot body) and the rear segment (i.e. robot tail), which are connected by dovetail slots. The minimal design concept relies on only one single actuator and two driven tendons that can contract alternatively, which reduces the design and fabrication complexity. The two tendons are wound respectively on a spindle in two opposite directions (figure 2(d)) so that when the motor rotates, regardless of the rotation direction, there is always one contracted and the other extended. With such an actuation mechanism, the middle segment (42.69 g, 92 × 28 × 20 mm) can produce a left and right oscillating wave bending motion. The front segment (6.98 g, 14 × 28 × 20 mm) can also swing left and right with the middle segment to provide the propelling force for locomotion. The robot head and body are both made of silicon rubber E605 (Hong Ye Silicone) by a mold-casting method (figure 2(c)). The two components E605 A and E605 B are thoroughly mixed with a ratio of 1:1 in a vacuum mixer. The prepared mixture is then poured into the three-dimensional (3D)-printed mold with two steel rods and cured in an incubator at 50 °C for at least 1 h. Steel rods in the robot body mold serve as placeholders for the tendons during the curing process and are removed once the silicone rubber mixture is cured. The rear part (28.06 g, 42 × 28 × 20 mm) serves as the robot actuation system, which consists of a motor holder, a spindle, two Kevlar driven tendons, two shafts for changing the tendon direction and a direct current (DC) motor N20 (figure 2(b)). The spindle is connected to the shaft of the DC motor. The motor holder and spindle are 3D printed with polylactic acid (PLA). The control system consists of an Arduino Uno, a motor-driven board L298N, and a DC-regulated power supply (figure 2(d)).

2.2. Material characterization

The mechanical properties of the soft materials for the SCR are measured for the mechanics analysis. The tensile test was performed for E605 elastomer using the Instron, following the protocol of ASTM D412-16 (standard test methods for vulcanized rubber and thermoplastic elastomers tension). Dumbbell-shaped specimens of the elastomer were prepared by the mold-casting method as described in the previous section for the robot body fabrication. The dimensions of the specimen are 4.2 × 12 × 35.88 mm. The strain rate for the tensile testing was set to 1 mm s^{-1}. Figure 3(d) shows the stress–strain curves of the E605 elastomer which exhibits a mild nonlinearity within 100% strain and a small hysteresis. The Young's modulus of E605 elastomer is estimated to be ∼50.4 kPa by fitting the stress–strain curve within 100% strain and will be used for the FEA simulation.

The dynamic friction coefficients of the SCR were further measured with a customized friction measurement platform on unstructured pipes made of different kinds of materials, including silicon rubber, sponge, polymethyl methacrylate (PMMA) and marble. Table 2 presents the measured dynamic friction coefficients between different material surfaces with the robot material PLA and silicon rubber E605. The friction-induced contact discontinuity may significantly affect the SCR's locomotion. To address this issue, a polymer gel layer was coated on the bottom of the SCR. The measured data for the dynamic friction coefficients with the gel layer are also shown in table 2.

2.3. Improved constant curvature model involving axial contraction

In the past decades, a few analytical models have been developed for the kinematic modeling of tendon-driven robots, such as the constant curvature model [39] and the geometrically exact beam theory [40]. The constant curvature model is the most adopted

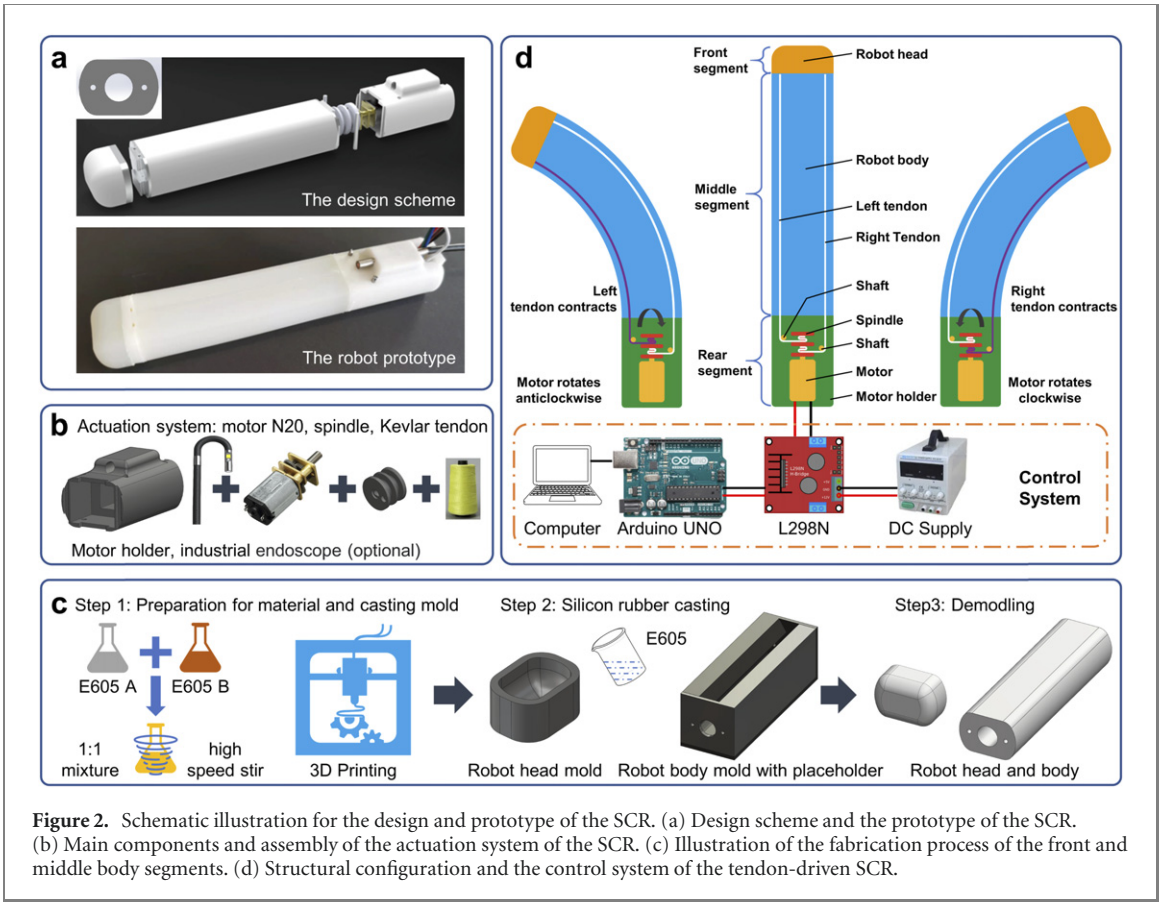

Figure 2. Schematic illustration for the design and prototype of the SCR. (a) Design scheme and the prototype of the SCR. (b) Main components and assembly of the actuation system of the SCR. (c) Illustration of the fabrication process of the front and middle body segments. (d) Structural configuration and the control system of the tendon-driven SCR.

Table 2. The dynamic friction coefficients between different material surfaces.

Robot material	Pipe material							
	PMMA	Marble	Sponge	Rubber	PMMA	Marble	Sponge	Rubber
	Without polymer gel layer				With polymer gel layer			
Rubber	2.79 ± 0.41	2.95 ± 0.35	1.54 ± 0.46	3.27 ± 0.23	1.91 ± 0.43	0.57 ± 0.10	1.16 ± 0.15	1.68 ± 0.17
PLA	1.68 ± 0.07	2.26 ± 0.18	0.76 ± 0.09	5.12 ± 0.35	1.64 ± 0.18	1.83 ± 0.21	0.97 ± 0.22	1.59 ± 0.20

Table 3. The physical quantities and symbols in the derivation.

Physical quantity	Symbol	Physical quantity	Symbol
Tendon force	F	The moment of inertia of cross section	I
The offset of tendon to central line	ξ	The area of body cross section	A
Young's modulus	E	Tendon contraction	Δx
Initial central line length	L	Deformed central line length	l
Initial axis configuration	s	Deformed axis configuration	S
Configuration of bending angle	θ	Bending angle of the robot	θ_0

model, which can significantly reduce the number of degrees of freedom from infinity to a few. The previous constant-curvature model neglects the axial contraction in the deformation of robots, which is applicable to the conventional rigid tendon-driven continuum robots with high axial stiffness. However, for the proposed SCR that has non-negligible axial contraction, the constant-curvature model should be improved by including the axial contraction in the modeling. The physical quantities and symbols used in the analytical derivation are shown in table 3.

The initial configuration and the deformed configuration with the free body diagram of the SCR are shown in figures 3(a) and (b). Without considering the gravity, the equilibrium equations of force and moment can be written as

$$F = EA\left(1 - \frac{l}{L}\right), \qquad F\xi = \left(EI\frac{l}{L}\right)\frac{\theta}{l}. \tag{1}$$

Substituting equation (1a) into equation (1b), the contraction of the central line is

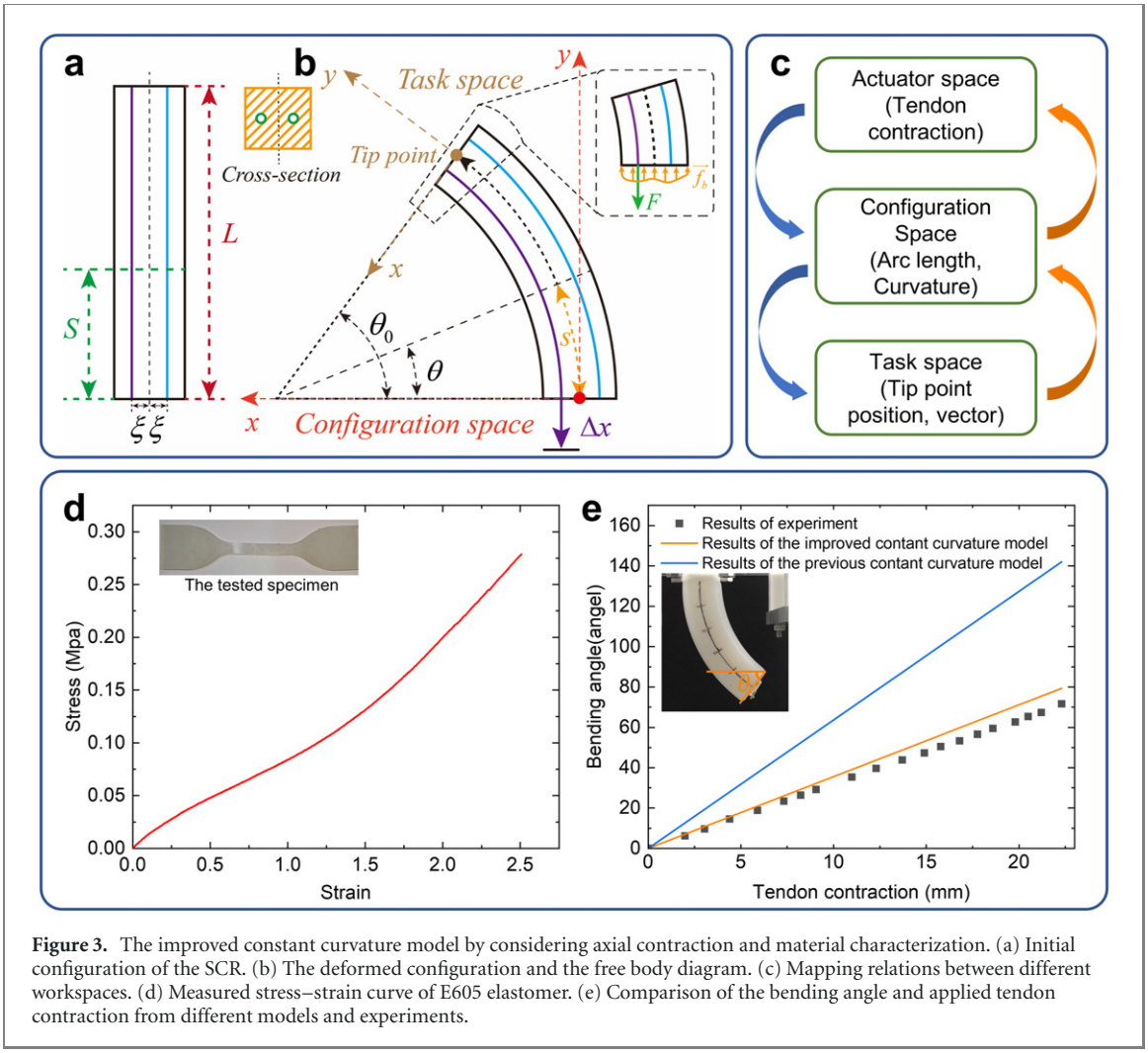

Figure 3. The improved constant curvature model by considering axial contraction and material characterization. (a) Initial configuration of the SCR. (b) The deformed configuration and the free body diagram. (c) Mapping relations between different workspaces. (d) Measured stress–strain curve of E605 elastomer. (e) Comparison of the bending angle and applied tendon contraction from different models and experiments.

$$L - l = \frac{I\theta_0}{A\xi}. \tag{2}$$

Geometrically, the length of the contracted tendon can be written as

$$l_d = l - \theta_0 \xi, \tag{3}$$

and the contraction of the driven tendon can be expressed as

$$\Delta x = L - (l - \theta_0 \xi) = \left(\frac{I}{A\xi} + \xi\right)\theta_0. \tag{4}$$

Substituting equation (4) into equation (2), the deformed central line length becomes

$$l = L - \frac{I}{I + A\xi^2}\Delta x. \tag{5}$$

Thus, the bending angle and the radius of the central line can be expressed as a function of the tendon contraction

$$\theta_0 = \frac{A\xi}{I + A\xi^2}\Delta x, \qquad r = \frac{l}{\theta_0} = \frac{(I + A\xi^2)L - I\Delta x}{A\xi\Delta x}. \tag{6}$$

In the configuration space of a planar case, the position vector of the tip point of the soft robot is

$$\vec{p} = (x, y)^{\mathrm{T}} = \left(1 - \cos\left(\frac{A\xi\Delta x}{I + A\xi^2}\right) \times \sin\left(\frac{A\xi\Delta x}{I + A\xi^2}\right)\right)^{\mathrm{T}} \frac{(I + A\xi^2)L - I\Delta x}{A\xi\Delta x}. \tag{7}$$

Then, the transformation relations between the different spaces are displayed in figure 3(c). The transformation matrix from the actuation space to the configuration space is the description of tendon contraction

$$\Delta x = v * t * R, \tag{8}$$

where v is the rotation speed of the motor, t is the rotation time and R is the radius of the spindle.

Given the above, the transformation matrix between the configuration space and the task space can be written as

$$T = \begin{bmatrix} R_y(\theta_0) & \vec{p} \\ 0 & 1 \end{bmatrix}, \quad R_y(\theta_0) = \begin{bmatrix} \cos(\theta_0) & -\sin(\theta_0) \\ \sin(\theta_0) & \cos(\theta_0) \end{bmatrix},$$
$$\vec{p} = (r(1 - \cos\theta_0), r\sin\theta_0). \tag{9}$$

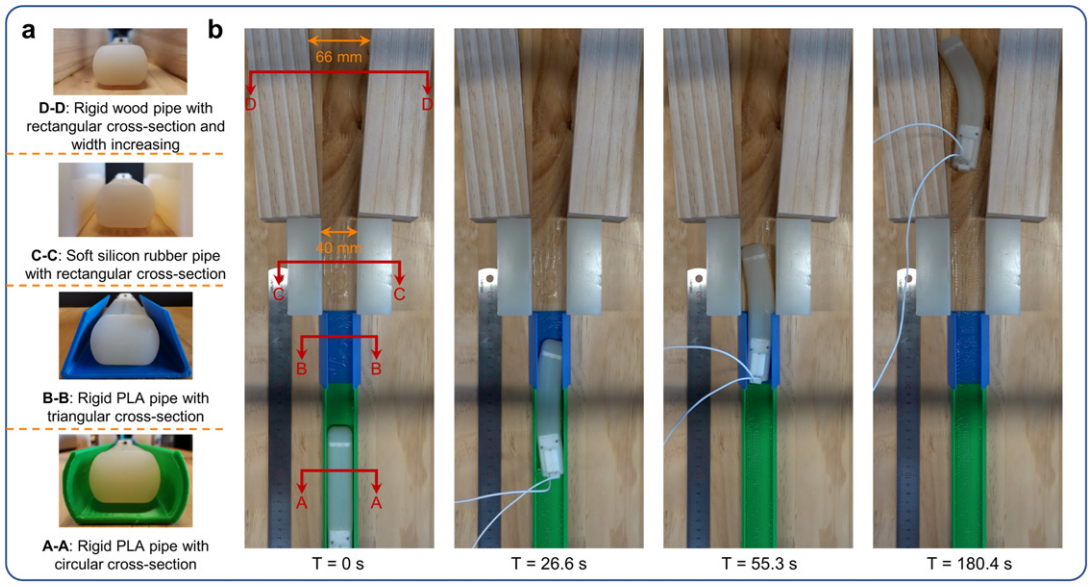

Figure 4. Locomotion performance of the SCR in the unstructured pipe. (a) The material and cross-section of different sections of the unstructured pipe. (b) Photos of the crawling locomotion in the unstructured pipe.

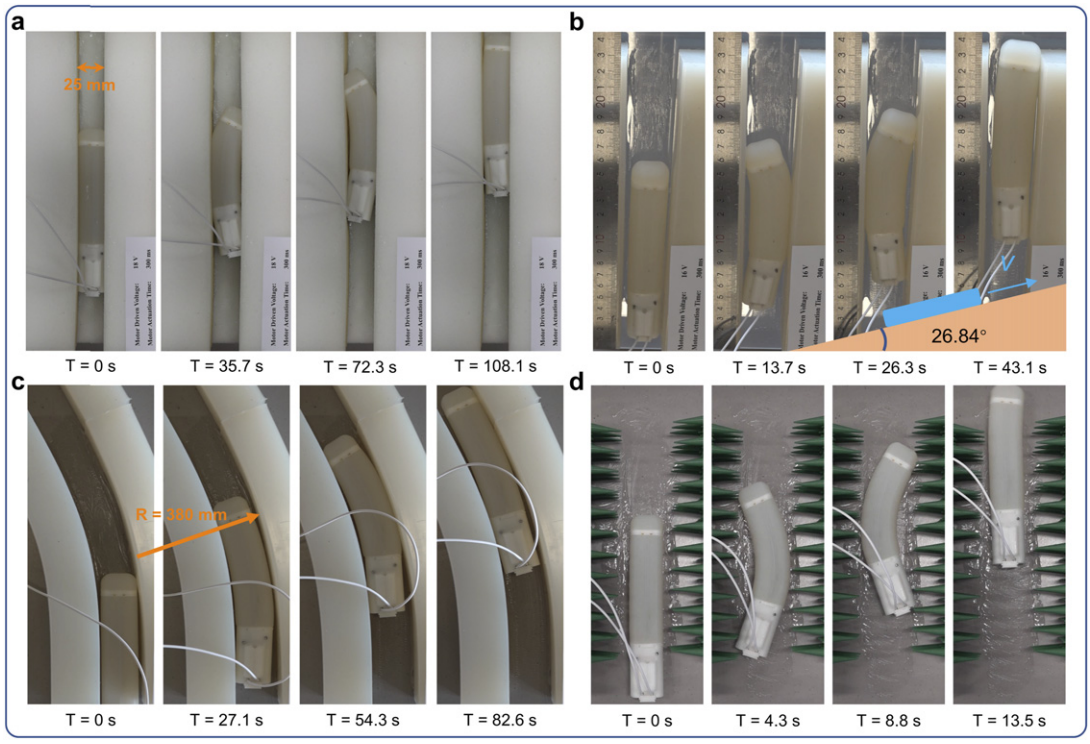

Figure 5. Adaptability performance of the SCR in different tubular environments. (a) Photos of the crawling locomotion in a soft pipe made of sponge, 25 mm wide. (b) Photos of the crawling locomotion in a pipe slope made of silicon rubber. (c) Photos of the crawling locomotion in a curved pipe with a radius of 380 mm. (d) Photos of the crawling locomotion in a spiked pipe.

To verify the improved constant curvature model, an experiment is performed to measure the bending angle of the SCR with the robot's end fixed. The results of the improved constant curvature model agree much better with experimental results, indicating that the improved accuracy in the description of the coupled robot deformation, as shown in figure 3(e). The error increased with tendon contraction because the cross section of the robot body and its geometric parameters, such as I and A, change

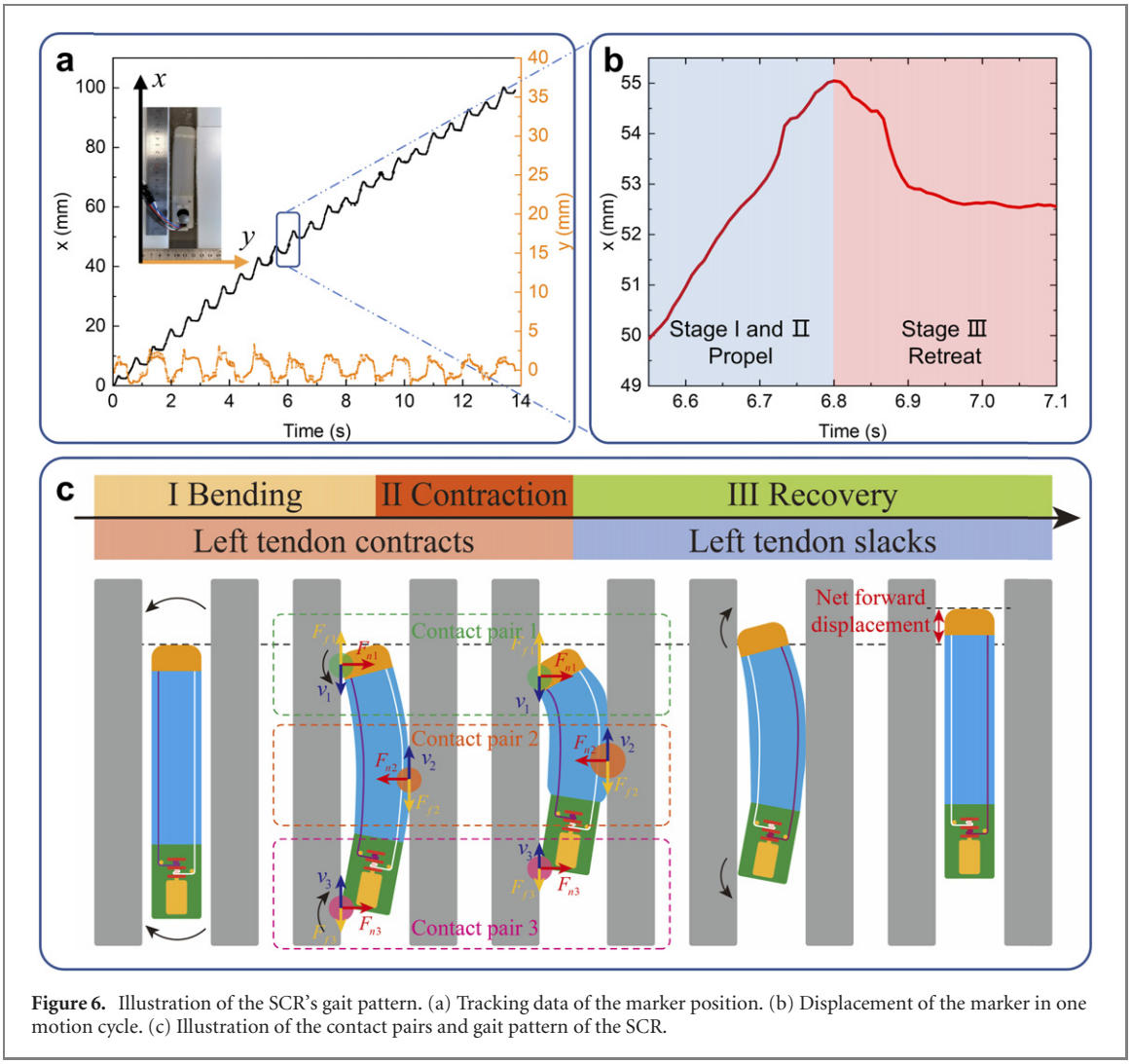

Figure 6. Illustration of the SCR's gait pattern. (a) Tracking data of the marker position. (b) Displacement of the marker in one motion cycle. (c) Illustration of the contact pairs and gait pattern of the SCR.

significantly during the deformation process due to the incompressible material property as it is compressed by the tendon force.

3. Experimental study for locomotion and gait pattern of the SCR

3.1. Locomotion performance of the SCR in unstructured pipes

Locomotion in unstructured pipes, especially in specific extreme conditions, remains a challenge for SCRs. In this section, the tendon-driven SCR is demonstrated as a promising solution in such conditions due to the efficient force transmission and adaptability of the new design. Figure 4 presents the locomotion of our SCR in an unstructured pipe comprising four different sections with variable parameters, like materials, the shape of the cross section and the width. The locomotion results show that SCR can effectively adapt to environmental changes (supplementary video S1 (https://stacks.iop.org/BB/17/056001/mmedia)).

3.2. Adaptability performance of the SCR

The adaptability to variable tubular environments is also critical to the SCR, as shown in figure 5. In soft pipes made of sponge, the SCR can propel well when the width of pipe varies from 25–38 mm (figure 5(a) and supplementary video S2). The SCR will become clamped when the pipe width is smaller than the robot BW (28 mm). The clamping force increases as the pipe width reduces. The clamping force reaches 2.5 N when the pipe width is 25 mm, about three times the SCR's gravity. Experiment results show that the SCR can propel in a soft pipe made of silicon rubber or rigid pipes made of iron or acrylic, with width varying from 30 mm to 80 mm. The SCR is also able to propel in tilted and curved pipes (figures 5(b) and (c) and supplementary videos S3 and S4). The experimental results validate that the maximum slope angle is 26.84° and the minimum turn radius is 380 mm. Remarkably, the SCR can move in hazardous environments such as a spiked pipe safely and effectively because the soft robot body is not susceptible to puncture damage (figure 5(d) and supplementary video S5). The load-carrying capacity

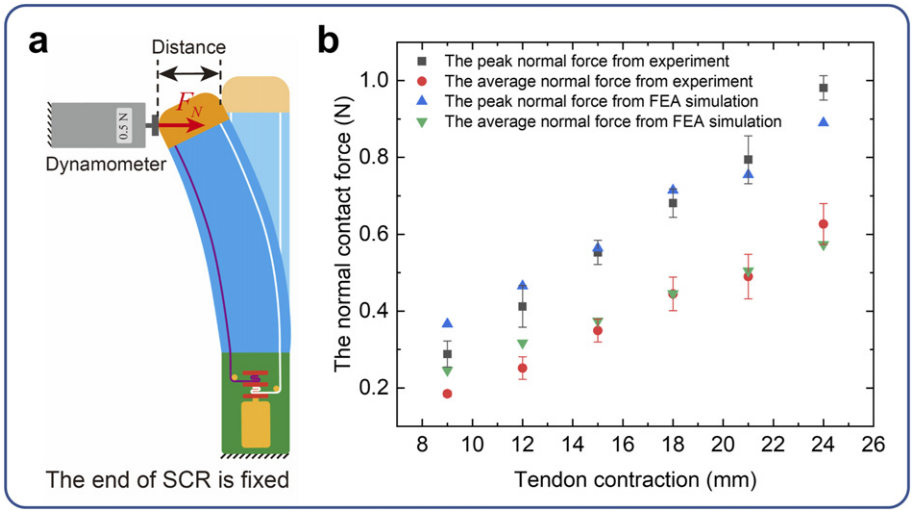

Figure 7. Measurement of the contact force between the SCR and the pipe. (a) Illustration of the force measurement. (b) Comparison between the experimental and simulation results.

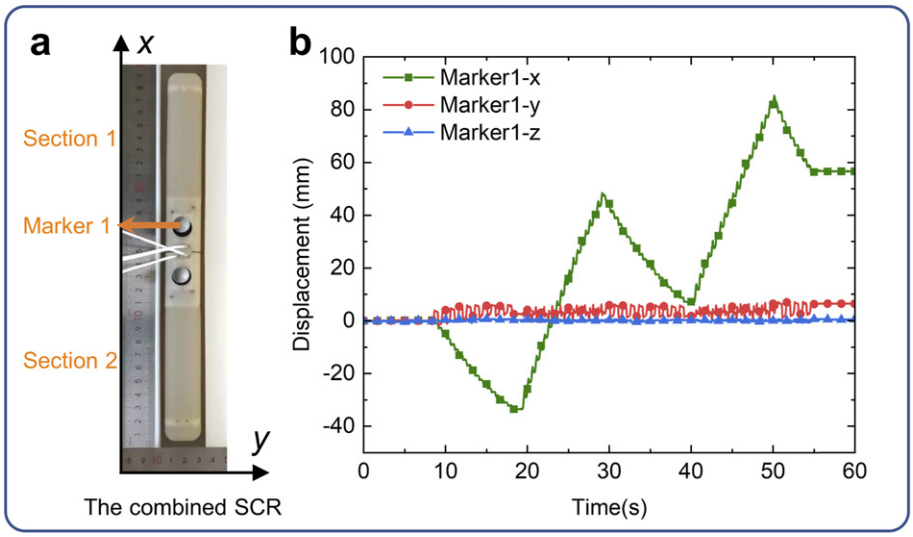

Figure 8. Bi-directional crawling locomotion of the combined SCR in a pipe. (a) The combined SCR with two sections. (b) Displacement of the marker 1 fixed on the SCR.

of the SCR performs well, up to 20 times the robot's weight (supplementary video S6). The widest pipe it can pass is up to 80 mm (2.85 times BW), as shown in supplementary video S7.

3.3. Illustration of the SCR's gait pattern

To investigate the gait pattern of the SCR, a motion capture system was used to track the displacement of the marker fixed on the shape center of the robot tail. As shown in figures 6(a) and (c), the locomotion process consists of many motion cycles, which can be further divided into three stages, including the bending, contraction and recovery stages. The bending stage starts from the initial straight condition and then bends to contact with the pipe surface. In this stage, the deformation is dominated by bending with negligible axial contraction, so 'bending' is used instead. The improved constant curvature model described above can be used to predict the deformed configuration. The contraction stage starts from the formation of contacts with pipe to the end of tendon contraction. Within this stage, the contracted deformation is dominated due to the obstruction of the pipe, and the SCR configuration is no longer a circular shape. The recovery stage begins from the point when the SCR bends in the opposite direction until it returns to its undeformed initial configuration.

Figure 6(b) illustrates the displacement of the shape center of the robot tail within one motion cycle. In the bending and contraction stages, along the x-direction, the marker moves forward 5 mm; while in the recovery stage, the marker retracts 2.5 mm, which is less than the advancement, so the SCR gains a net

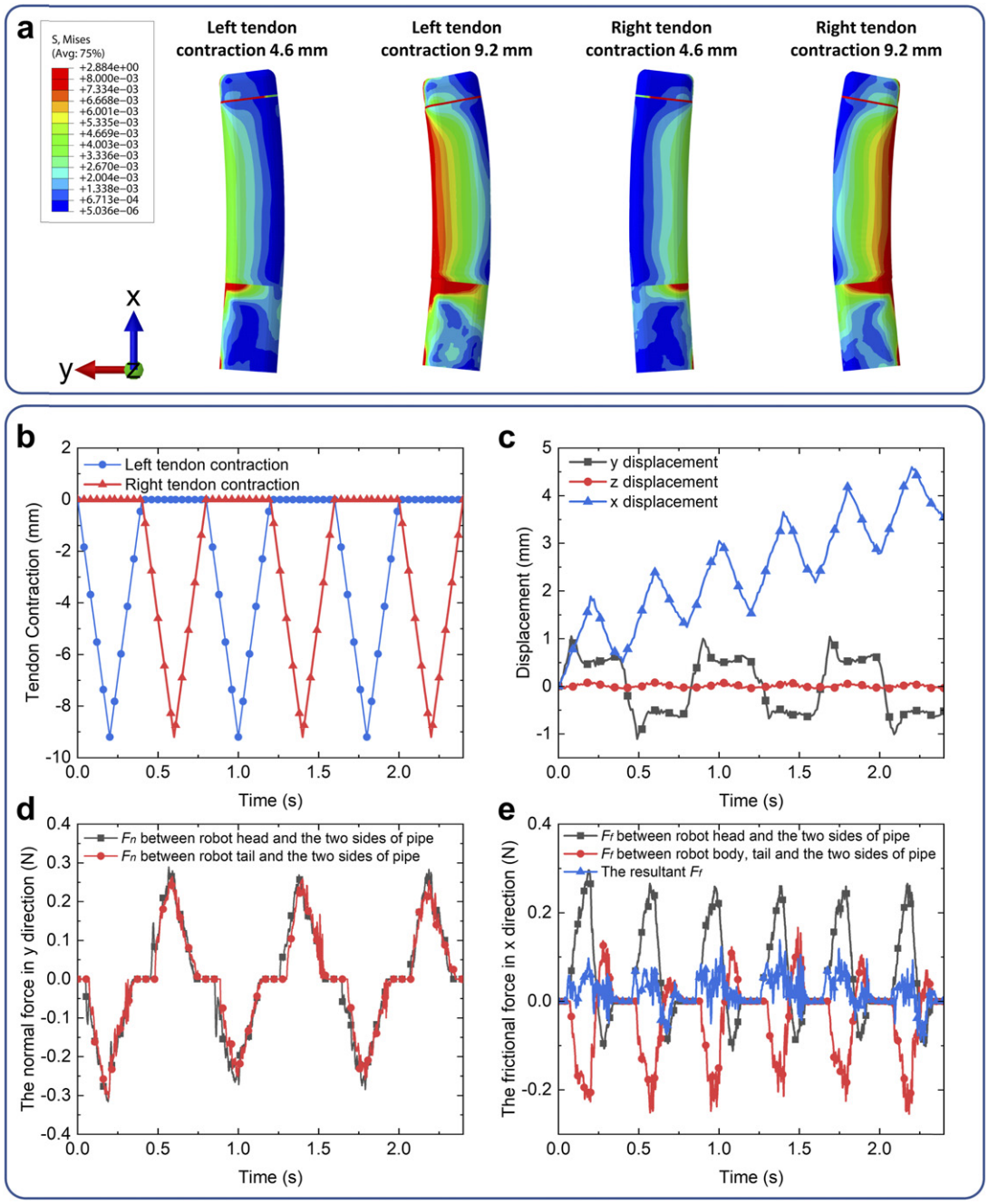

Figure 9. FEA simulation results of the SCR's locomotion. (a) Stress contour plots of the SCR deformation. (b) Actuated tendon contraction applied during the simulation. (c) Displacement of the shape center of the robot tail. (d) Normal contact force of the contact pairs. (e) Frictional force of the contact pairs.

forward displacement of 2.5 mm in each motion cycle. The forward propulsion is caused by the forward resultant frictional force exerted on the SCR, which will be discussed in section 4.

3.4. Measurement of the normal contact force between the SCR and the pipe

The contact between the SCR and the pipe plays a significant role in the locomotion of the SCR, which also provides insightful data into the robot design and optimization. Therefore, an experiment is performed to measure the peak and average normal force in the deformation process, where the end of the SCR is fixed, the normal contact force is measured with a dynamometer and the distance between the SCR and the dynamometer is 5 mm, as shown in figure 7(a). As shown in figure 7(b), the contact force increases with tendon contraction, and the experimental results agree well with the FEA simulation, indicating that the simulation is credible.

3.5. Bi-directional locomotion of the SCR

Our minimal SCR can locomote in one direction because of the fixed asymmetric mechanical design. However, it can be extended to be a modular design by assembling multiple segment modules to form a

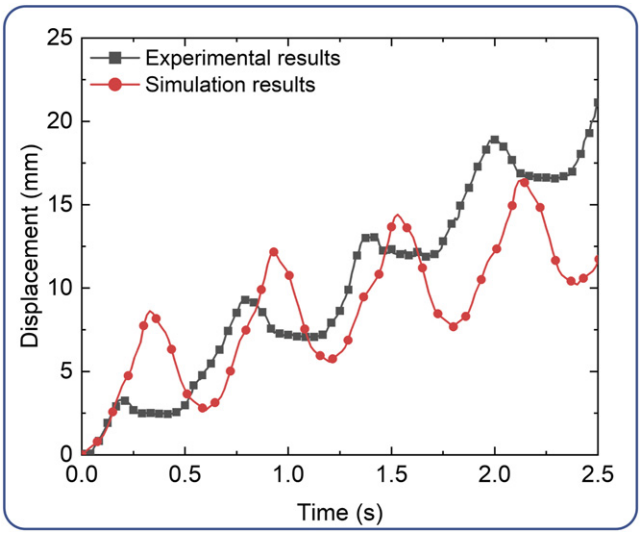

Figure 10. Comparison between the experimental and simulation results of the SCR's displacement under the same working conditions.

multi-segmented crawling robot. For instance, when two SCRs are assembled, the new combined SCR can perform bi-directional locomotion, as shown in figure 8 and supplementary video S8. The multi-segmented (⩾3 sections) SCR with sophisticated gait patterns will be studied in future work.

4. Finite element analysis of the locomotion process

SCRs undergo large strains and rotations that are difficult to model analytically. FEA can recapitulate the mechanics of robot behavior *in silico*, so as to provide an insightful understanding of the SCR's behavior (deformation and locomotion). Thus, a 3D FEA simulation of the SCR was performed by using the software package of ABAQUS/Explicit (DassaultSystèmes) and the C3D8T element. The geometry, material properties and contact interactions are considered in the models to simulate the complexity of the robot–environment interaction. The cross section of the pipe is rectangular and the width is 32 mm. In particular, the tendon contraction is implemented in ABAQUS by applying a temperature field to impose an eigen strain on the tendon material.

The SCR has three contact pairs (contact pair 1, 2 and 3) with the pipe sidewalls while propelling, as shown in figure 6(b). The resultant force of the three contact pairs determines the locomotion of the SCR since the robot can only propel when it has contact with the side of pipes. For the tangential behavior of contact, the friction formulation method is a penalty, which permits relative motion of the contact surfaces. The dynamic friction coefficients for three contact pairs are set as 1.0 with isotropic directionality. The normal force is denoted by F_n, and the tangential force (the frictional force) is denoted by F_f, which will be computed in the FEA simulation.

The FEA simulation results of the SCR's locomotion are as shown in figure 9 and supplementary video S9. Figure 9(a) presents the stress contour plots and deformation profiles of the SRC when the two tendons are respectively contracted as shown in figure 9(b). By applying the thermal strain, the tendon contraction is well controlled and increases linearly to the maximum and then restores to the original length. Figure 9(c) shows the displacement curve of the point positioned on the robot tail's shape center, the trend of which agrees well with the experimental results. The normal contact force and the tangential contact force generated between the SCR and the side walls are shown in figures 9(d) and (e), respectively. It can be seen that the contact force increases continuously as tendon contraction, which agrees well with the measured normal force shown in figure 7. The weight, segment length, actuation and Young's modulus of the SCR's front segment are different from those of the rear segment. It is interpreted that the asymmetric mechanical properties of the SCR cause the asymmetric contact force in the locomotion process, i.e. the friction force F_{f1} is larger than the resultant of F_{f2} and F_{f3}, thus the SCR gets an unbalanced forward frictional force to move forward, as shown in figure 9(e). More comprehensive computational modeling of the contact problem identifying the exact factors that lead to asymmetric forces will be carried out in future work.

It can be seen that there is a discrepancy between the simulation results (figure 9(c)) and the experimental results (figure 6(a)) of the SCR's displacement in the x-direction, which is caused by the unmatched working conditions. In the crawling locomotion described in figure 6, the width of the pipe is 36 mm, and the friction coefficients of the three

contact pairs are 3.5, 0.2 and 0.2, respectively. While in the FEA simulation mentioned above, the width of the pipe is 32 mm and the friction coefficients are all 1.0. The discrepancy can be reduced by adjusting the simulation parameters to match the experimental conditions, which provides quantitative verification of the FEA simulation, as shown in figure 10.

5. Conclusion

In this work, a tendon-driven SCR is proposed for effective and robust locomotion in unstructured pipes. With one single actuation unit, the minimalist SCR can generate a left and right bending gait pattern. An extensive locomotion study demonstrated that the novel SCR could propel in unstructured pipes with variable geometrical and material properties and surface topology. The driving force for the locomotion is the unbalanced forward friction due to the asymmetric mechanical properties along the length direction of the SCR, which has been verified through an FEA simulation. This research provides a feasible solution for extending soft robots to broader applications in unstructured pipes, such as interventional medical and pipeline inspection. In the future, the minimalist SCR could be further extended to a modular design, which could be conveniently assembled to form a complex multiple segment SCR with different kinds of configurations for specific applications. It is anticipated that the new combined SCR can perform more sophisticated gait patterns and locomotion strategies with the modular extension.

Acknowledgments

The authors would like to acknowledge the funding support from the National Natural Science Foundation of China (Grant Nos. 12072143, 12172160), the Stable Support Plan Program of Shenzhen Natural Science Fund (Grant No. 20200925155345003), and the Science, Technology and Innovation Commission of Shenzhen Municipality (Grant No. ZDSYS20210623092005017).

Data availability statement

No new data were created or analyzed in this study.

Conflict of interest

No competing financial interests exist.

ORCID iDs

Hongyan Yuan https://orcid.org/0000-0001-8225-0211

References

[1] Rus D and Tolley M T 2015 Design, fabrication and control of soft robots *Nature* **521** 467–75
[2] Tolley M T, Shepherd R F, Mosadegh B, Galloway K C, Wehner M, Karpelson M, Wood R J and Whitesides G M 2014 A resilient, untethered soft robot *Soft Robot.* **1** 213–23
[3] Roche E T *et al* 2017 Soft robotic sleeve supports heart function *Sci. Trans. Med.* **9** eaaf3925
[4] Polygerinos P, Wang Z, Galloway K C, Wood R J and Walsh C J 2015 Soft robotic glove for combined assistance and at-home rehabilitation *Robot. Auton. Syst.* **73** 135–43
[5] Chen S, Cao Y, Sarparast M, Yuan H, Dong L, Tan X and Cao C 2020 Soft crawling robots: design, actuation, and locomotion *Adv. Mater. Technol.* **5** 1900837
[6] Bernth J E, Arezzo A and Liu H 2017 A novel robotic meshworm with segment-bending anchoring for colonoscopy *IEEE Robot. Autom. Lett.* **2** 1718–24
[7] Liu X, Song M, Fang Y, Zhao Y and Cao C 2021 Worm-inspired soft robots enable adaptable pipeline and tunnel inspection *Adv. Intell. Syst.* **4** 2100128
[8] Verma M S, Ainla A, Yang D, Harburg D and Whitesides G M 2018 A soft tube-climbing robot *Soft Robot.* **5** 133–7
[9] Zhang B, Fan Y, Yang P, Cao T and Liao H 2019 Worm-like soft robot for complicated tubular environments *Soft Robot.* **6** 399–413
[10] Yeh C-Y, Chou S-C, Huang H-W, Yu H-C and Juang J-Y 2019 Tube-crawling soft robots driven by multistable buckling mechanics *Extreme Mech. Lett.* **26** 61–8
[11] Ge J Z, Calderón A A, Chang L and Pérez-Arancibia N O 2019 An earthworm-inspired friction-controlled soft robot capable of bidirectional locomotion *Bioinsp. Biomim.* **14** 036004
[12] Fang H, Zhang Y and Wang K W 2017 Origami-based earthworm-like locomotion robots *Bioinsp. Biomim.* **12** 065003
[13] Yeh C-Y, Chen C-Y and Juang J-Y 2020 Soft hopping and crawling robot for in-pipe traveling *Extreme Mech. Lett.* **39** 100854
[14] Dong X, Tang C, Jiang S, Shao Q and Zhao H 2021 Increasing the payload and terrain adaptivity of an untethered crawling robot via soft-rigid coupled linear actuators *IEEE Robot. Autom. Lett.* **6** 2405–12
[15] Xie R, Su M, Zhu H and Guan Y 2019 A 2D pneumatic soft robot with suckers for locomotion *2019 IEEE Int. Conf. on Robotics and Biomimetics (ROBIO)* pp 1325–30
[16] Gu G, Zou J, Zhao R, Zhao X and Zhu X 2018 Soft wall-climbing robots *Sci. Robot.* **3** eaat2874
[17] Qin L, Liang X, Huang H, Chui C K, Yeow R C-H and Zhu J 2019 A versatile soft crawling robot with rapid locomotion *Soft Robot.* **6** 455–67
[18] Liu B, Ozkan-Aydin Y, Goldman D I and Hammond F L 2019 Kirigami skin improves soft earthworm robot anchoring and locomotion under cohesive soil *2019 2nd IEEE Int. Conf. on Soft Robotics (RoboSoft)* pp 828–33
[19] Rafsanjani A, Zhang Y, Liu B, Rubinstein S M and Bertoldi K 2018 Kirigami skins make a simple soft actuator crawl *Sci. Robot.* **3** eaar7555
[20] Wen L, Weaver J C and Lauder G V 2014 Biomimetic shark skin: design, fabrication and hydrodynamic function *J. Exp. Biol.* **217** 1656–66
[21] Tang Y, Chi Y, Sun J, Huang T-H, Maghsoudi O H, Spence A, Zhao J, Su H and Yin J 2020 Leveraging elastic instabilities for amplified performance: spine-inspired high-speed and high-force soft robots *Sci. Adv.* **6** eaaz6912
[22] Yang Y, Tse Y A, Zhang Y, Kan Z and Wang M Y 2019 A low-cost inchworm-inspired soft robot driven by supercoiled polymer artificial muscle *2019 2nd IEEE Int. Conf. on Soft Robotics (RoboSoft)* pp 161–6
[23] Wang W, Lee J-Y, Rodrigue H, Song S-H, Chu W-S and Ahn S-H 2014 Locomotion of inchworm-inspired robot

made of smart soft composite (SSC) *Bioinsp. Biomim.* **9** 046006
[24] Umedachi T, Vikas V and Trimmer B A 2016 Softworms : the design and control of non-pneumatic, 3D-printed, deformable robots *Bioinsp. Biomim.* **11** 025001
[25] Wang N, He M, Cui Y, Sun Y and Qi P 2020 A soft pneumatic crawling robot with unbalanced inflation *2020 IEEE/ASME Int. Conf. on Advanced Intelligent Mechatronics (AIM)* pp 138–43
[26] Qi X, Shi H, Pinto T and Tan X 2020 A novel pneumatic soft snake robot using traveling-wave locomotion in constrained environments *IEEE Robot. Autom. Lett.* **5** 1610–7
[27] Drory L-H and Zarrouk D 2019 Locomotion dynamics of a miniature wave-like robot, modeling and experiments *2019 Int. Conf. on Robotics and Automation (ICRA)* pp 8422–8
[28] Banerjee H, Pusalkar N and Ren H 2018 Preliminary design and performance test of tendon-driven origami-inspired soft peristaltic robot *2018 IEEE Int. Conf. on Robotics and Biomimetics (ROBIO)* pp 1214–9
[29] Kastor N, Mukherjee R, Cohen E, Vikas V, Trimmer B A and White R D 2020 Design and manufacturing of tendon-driven soft foam robots *Robotica* **38** 88–105
[30] Vikas V, Cohen E, Grassi R, Sozer C and Trimmer B 2016 Design and locomotion control of a soft robot using friction manipulation and motor-tendon actuation *IEEE Trans. Robot.* **32** 949–59
[31] Gilbertson M D, McDonald G, Korinek G, Van de Ven J D and Kowalewski T M 2017 Serially actuated locomotion for soft robots in tube-like environments *IEEE Robot. Autom. Lett.* **2** 1140–7
[32] Pham L N and Abbott J J 2018 A soft robot to navigate the lumens of the body using undulatory locomotion generated by a rotating magnetic dipole field *2018 IEEE/RSJ Int. Conf. on Intelligent Robots and Systems (IROS)* (Piscataway, NJ: IEEE) pp 1783–8
[33] Kim Y, Parada G A, Liu S and Zhao X 2019 Ferromagnetic soft continuum robots *Sci. Robot.* **4** eaax7329
[34] Niu H, Feng R, Xie Y, Jiang B, Sheng Y, Yu Y, Baoyin H and Zeng X 2021 MagWorm: a biomimetic magnet embedded worm-like soft robot *Soft Robot.* **8** 507–18
[35] Amanov E, Nguyen T-D and Burgner-Kahrs J 2019 Tendon-driven continuum robots with extensible sections—a model-based evaluation of path-following motions *Int. J. Robot. Res.* **40** 7
[36] Chen S, Pang Y, Yuan H, Tan X and Cao C 2020 Smart soft actuators and grippers enabled by self-powered tribo-skins *Adv. Mater. Technol.* **5** 1901075
[37] Zarrouk D, Sharf I and Shoham M 2012 Conditions for worm-robot locomotion in a flexible environment: theory and experiments *IEEE Trans. Biomed. Eng.* **59** 1057–67
[38] Zhang X, Pan T, Heung H L, Chiu P W Y and Li Z 2018 A biomimetic soft robot for inspecting pipeline with significant diameter variation *2018 IEEE/RSJ Int. Conf. on Intelligent Robots and Systems (IROS)* pp 7486–91
[39] Webster R J and Jones B A 2010 Design and kinematic modeling of constant curvature continuum robots: a review *Int. J. Robot. Res.* **29** 1661–83
[40] Li X, Yu W, Baghaee M, Cao C, Chen D, Liu J and Yuan H 2022 Geometrically exact finite element formulation for tendon-driven continuum robots *Acta Mech. Solida Sin.*